molecules

MDPI

Article

Efficient Selective Capture of Carbon Dioxide from Nitrogen and Methane Using a Metal-Organic Framework-Based Nanotrap

Junjie Peng [1], Chengmin Fu [1], Jiqin Zhong [2], Bin Ye [3], Jing Xiao [4], Chongxiong Duan [5] and Daofei Lv [1,*]

[1] School of Environmental and Chemical Engineering, Foshan University, Foshan 528000, China; cepengjunjie@fosu.edu.cn (J.P.); callinia@foxmail.com (C.F.)
[2] GAC R&D Center, Guangzhou Automobile Group Co., Ltd., 668 Jinshan Road East, Panyu District, Guangzhou 511434, China; jackingzhong@163.com
[3] Appraisal Center for Environment and Engineering, Ministry of Ecology and Environment, Beijing 100012, China; yebin@acee.org.cn
[4] School of Chemistry and Chemical Engineering, South China University of Technology, Guangzhou 510640, China; cejingxiao@scut.edu.cn
[5] School of Materials Science and Hydrogen Engineering, Foshan University, Foshan 528000, China; cechxduan@fosu.edu.cn
* Correspondence: lvdaofei@fosu.edu.cn

Abstract: Selective carbon capture from exhaust gas and biogas, which mainly involves the separation of CO_2/N_2 and CO_2/CH_4 mixtures, is of paramount importance for environmental and industrial requirements. Herein, we propose an interesting metal-organic framework-based nanotrap, namely $ZnAtzCO_3$ (Atz^- = 3-amino-1,2,4-triazolate, CO_3^{2-} = carbonate), with a favorable ultramicroporous structure and electrostatic interactions that facilitate efficient capture of CO_2. The structural composition and stability were verified by FTIR, TGA, and PXRD techniques. Particularly, $ZnAtzCO_3$ demonstrated high CO_2 capacity in a wide range of pressures, with values of 44.8 cm^3/g at the typical CO_2 fraction of the flue gas (15 kPa) and 56.0 cm^3/g at the CO_2 fraction of the biogas (50 kPa). Moreover, ultrahigh selectivities over CO_2/N_2 (15:85, *v:v*) and CO_2/CH_4 (50:50, *v:v*) of 3538 and 151 were achieved, respectively. Molecular simulations suggest that the carbon atom of CO_2 can form strong electrostatic $C^{\delta+}\ldots^{\delta-}O$-C interactions with four oxygen atoms in the carbonate ligands, while the oxygen atom of CO_2 can interact with the hydrogen atoms in the triazolate ligands through $O^{\delta-}\ldots^{\delta+}H$-C interactions, which makes $ZnAtzCO_3$ an optimal nanotrap for CO_2 fixation. Furthermore, breakthrough experiments confirmed excellent real-world separation toward CO_2/N_2 and CO_2/CH_4 mixtures on $ZnAtzCO_3$, demonstrating its great potential for selective CO_2 capture.

Keywords: metal-organic framework; CO_2 capture; nanotrap; gas separation

check for updates

Citation: Peng, J.; Fu, C.; Zhong, J.; Ye, B.; Xiao, J.; Duan, C.; Lv, D. Efficient Selective Capture of Carbon Dioxide from Nitrogen and Methane Using a Metal-Organic Framework-Based Nanotrap. *Molecules* **2023**, *28*, 7908. https://doi.org/10.3390/molecules28237908

Academic Editor: Emilio Pardo

Received: 16 November 2023
Revised: 30 November 2023
Accepted: 30 November 2023
Published: 2 December 2023

1. Introduction

Global warming, one of the biggest global issues, is causing various long-term disastrous environmental effects, including abnormal climate patterns, rising sea levels, accelerated extinction of species, and shifts in agricultural patterns, which pose severe threats to the survival and development of humanity [1–4]. As the main source of greenhouse gases, carbon dioxide (CO_2), with a large annual emission (e.g., 36.8 Gt in 2022), contributes to 69.4% of the anthropogenic greenhouse gases [5,6]. Hence, CO_2 capture and utilization is of utmost importance to curb global warming [7]. In particular, electricity generation from the combustion of fossil fuels, resulting in exhaust gas composed mainly of CO_2 and nitrogen (N_2), is the primary source of anthropogenic CO_2 emissions [8,9]. Additionally, biogas, acknowledged as "renewable natural gas", is a green fuel with the efficient component of methane (CH_4) [10]. Nevertheless, biogas contains a considerable amount of CO_2 that could significantly decrease the calorific value and lead to severe erosion in the equipment. Therefore, efficient selective capture of CO_2 from N_2 and CH_4 is of paramount significance for environmental protection and biogas upgrading.

Benefiting from a plausible gentle operation condition and reduced energy consumption for regeneration, adsorptive separation of CO_2 has been recognized as a promising alternative among the current CO_2 capture techniques [11–14]. Fundamentally, an ideal adsorbent with high capacity and selectivity for the target molecule is the key to achieving satisfactory separation performance [15,16]. As a class of innovative porous adsorbents, metal-organic frameworks (MOFs) are showing extraordinary versatility in pore tunability and chemical functionalities [17]. Hence, adsorptive separation based on MOFs has been explored in miscellaneous separation circumstances, including carbon capture [8,9,11,18–20]. In general, there are several strategies that can enhance the CO_2 capture performance on MOF materials, including (i) incorporation of functionalities (such as open metal sites, Lewis basic sites, and polar functional groups) into the frameworks, (ii) utilization of ultramicropores to maximize the confinement effect, (iii) use of kinetic difference and even the molecular sieving effect, (iv) introduction of structural flexibility, (v) the combination thereof [16,21,22]. Specifically, MOFs constructed by triazolate linkers represent one subclass of MOFs that are comprised of excellent CO_2 capture performance, affordable costs, and good stability under humid conditions [23,24]. For example, by introducing amino groups into the triazolate linkers of the prototype MOF ZnF(TZ), the resultant ZnF(daTZ) demonstrates an appreciable volumetric CO_2 uptake of 75 cm^3/cm^3 and high CO_2/N_2 equilibrium selectivity of 120 based on the ideal adsorbed solution theory (IAST) as well as excellent CO_2/H_2O kinetic selectivity of 70 [25]. This remarkable separation performance was probably originated from the main adsorptive site at the channel center for CO_2 to afford electrostatic interactions with the amino groups, while H_2O was more likely to locate at the channel corner, according to GCMC simulations. Built from dual ligands of oxalate and 1,2,4-triazolate, zinc-based Calgary Framework 20 (CALF-20) exhibits a high CO_2 capacity of 87.36 cm^3/g at atmospheric conditions, excellent selectivities over N_2 and H_2O, and the facility for scalable production, making it the first practical MOF for industrial carbon capture [26,27]. Molecular simulations suggest the CO_2 adsorption location in CALF-20 also lies in the channel center to form interactions with the zinc/nitrogen/carbon atoms in the framework. Likewise, the amine-appended zinc-oxalate-triazolate MOFs demonstrated enhanced CO_2 capacity at low CO_2 concentrations compared to CALF-20, due to higher-density interaction sites and more contracted pore sizes [28,29]. Recently, we prepared a flexible MOF, namely ZnDatzBdc, that showed step-shaped CO_2 isotherm due to breakage/reformation of intra-framework hydrogen bonds and rotation of the phenyl rings, giving rise to an excellent CO_2 theoretical working capacity of 94.9 cm^3/cm^3 if performed in typical pressure vacuum swing adsorption at 273 K [30].

By now, developing nanotraps with multiple host-guest interactions toward the target molecules offers a feasible strategy to accomplish high adsorption capacity and selectivity, which has been successfully applied in separation circumstances, such as C_2H_2/CO_2 separation [31,32], C_3H_4/C_3H_6 separation [33,34], CH_4/N_2 separation [35], and olefin/paraffin separation [36]. For CO_2 adsorption, if a contracted pore exhibits opposite electrostatics on the adjacent positions and the same electrostatics on its opposite side, it can form strong electrostatic interactions with both the carbon and oxygen atoms in the CO_2 molecule, as shown in Figure 1. Hence, this type of pore can act as a suitable nanotrap for CO_2 fixation, from which a remarkable capacity and selectivity for CO_2 can be achieved.

Herein, we synthesized a novel MOF, namely $ZnAtzCO_3$, with 3-amino-1,2,4-triazolate (Atz^-) and carbonate (CO_3^{2-}) as dual ligands. Inspiringly, $ZnAtzCO_3$ shows the desired ultramicropores due to the small-sized ligands and suitable crystal structure, which is desirable for the adsorption and separation of small molecules, such as CO_2. Moreover, the favorable electrostatic environment of $ZnAtzCO_3$ makes it a feasible nanotrap to form multiple host-guest interactions with CO_2, and hence, efficient CO_2 capture from N_2 and CH_4 could be achieved. In particular, at atmospheric temperature, equilibrium isotherms showed high CO_2 capacities of $ZnAtzCO_3$ in a wide pressure range, with values of 44.8 cm^3/g (STP, standard temperature and pressure) at the typical fraction of the flue gas (15 kPa) and

56.0 cm^3/g at the fraction of the biogas (50 kPa). Moreover, adsorptive selectivity based on the IAST model indicated that ultra-high CO_2/N_2 and CO_2/CH_4 selectivities of 3538 and 151 were realized at ambient conditions, respectively. The excellence in capacity and selectivity of this MOF-based nanotrap was illustrated by molecular simulations in terms of preferential adsorption sites, binding energy, and adsorption distributions. Furthermore, breakthrough experiments toward the binary mixtures of CO_2/N_2 and CO_2/CH_4 were conducted on $ZnAtzCO_3$, which verified its efficient dynamic separation performance.

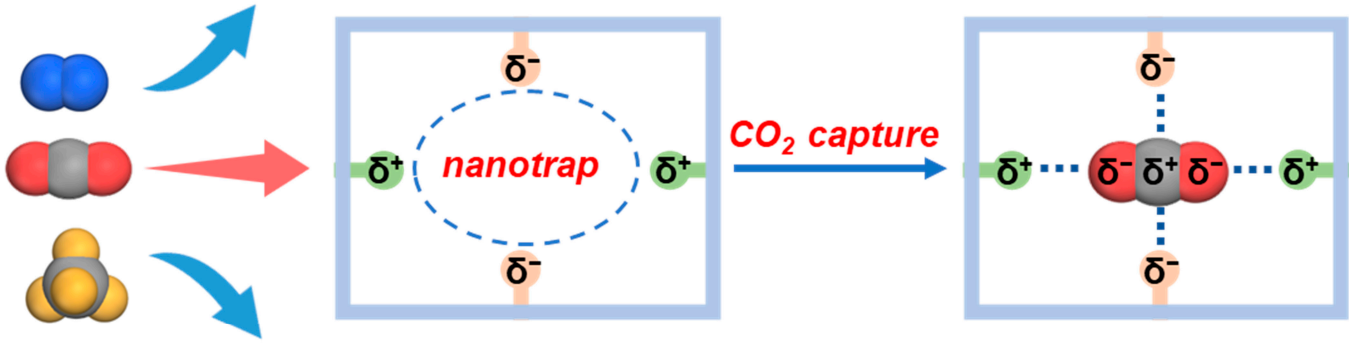

Figure 1. Selective CO_2 capture from N_2 and CH_4 on a nanotrap with a suitable electrostatic environment via multiple host–guest interactions. The blue dotted lines represent the electrostatic interactions between the framework and the CO_2 molecule.

2. Results and Discussion

2.1. Crystal Structure and Pore Properties

Reactions of $ZnSO_4$ and 3-amino-1*H*-1,2,4-triazole (HAtz) in a binary solution of DMF/H_2O afforded high-quality crystals of $ZnAtzCO_3$. The single-crystal X-ray diffraction (SCXRD) measurement indicates that $ZnAtzCO_3$ belongs to the triclinic crystal system (a = 9.6217 Å, b = 9.6316 Å, c = 16.3408 Å, α = 81.355°, β = 86.938°, γ = 76.093°). Each asymmetric unit contains four zinc atoms, four 3-aminotriazolate ligands, and two triangular carbonate linkers (Figure S1). Because no carbonate was added to the reactants, it is assumed that the carbonate linker originated from the decomposition of the DMF molecule [37]. In addition, the elemental analysis suggests no sulfur element in the framework, which further confirms the existence of the carbonate linker instead of the sulfate or sulfite linker in the framework. As shown in Figure 2a, the zinc atom coordinates with one oxygen atom from the carbonate linker and three nitrogen atoms from three different triazolate rings. Each carbonate linker contains one uncoordinated oxygen atom, which is fixed by the intra-framework hydrogen bonding with the amino group in the triazolate ligand. We tried to obtain isoreticular structures by replacing the HAtz ligand with 1*H*-1,2,4-triazole (HTz) and 3,5-diamine-1*H*-1,2,4-triazole (HDatz), but the trial failed. Hence, we assume that these weak intra-framework hydrogen bonds are vital for the structural formation of $ZnAtzCO_3$. $ZnAtzCO_3$ can be regarded as a pillared–layered structure by connecting the wavy and continuous zinc-triazolate layers by the carbonate pillars (Figure 2b). Inspiringly, the small size of the carbonate and triazolate ligands gives rise to an ultramicroporous structure desirable for adsorptive separation. Specifically, $ZnAtzCO_3$ contains two types of zig-zag channels with a cross-section area of 2.9 × 5.1 $Å^2$ and 3.5 × 5.1 $Å^2$ that interconnect with the adjacent channels through small apertures of 3.0 × 3.9 $Å^2$, 2.2 × 2.8 $Å^2$, and 2.6 × 3.3 $Å^2$. We noticed that a similar form of $Zn_2(atz)_2(CO_3)$ was previously reported by the reaction of $Zn(NO_3)_2$, $NaHCO_3$, and HAtz. $Zn_2(atz)_2(CO_3)$ displayed the same connectivity but belonged to another different space group of a Pnma unit cell (a = 9.806 Å, b = 9.3353 Å, c = 16.194 Å, $\alpha = \beta = \gamma = 90°$) [38]. The difference in structure is probably because the degrees of buckling for zinc-triazolate layers can vary significantly under different synthetic conditions. Because the specific crystal structure affects the pore systems and, subsequently, the sorption behavior, the following discussion was carried out with our obtained crystal data.

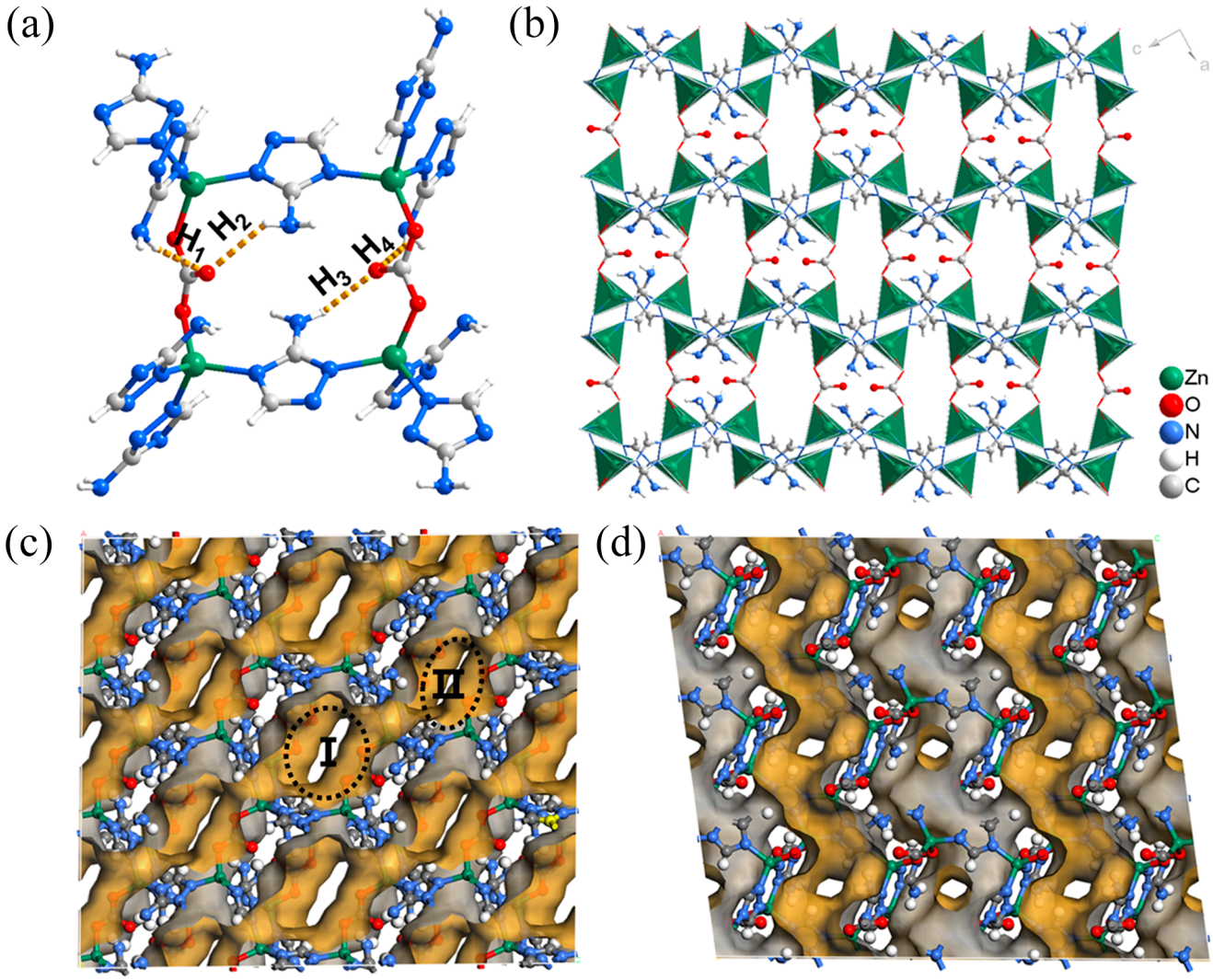

Figure 2. The crystal structure and pore property of $ZnAtzCO_3$: (**a**) coordination mode, (**b**) crystal structure shown in the b-axis, and the Connolly surface in the b-axis (**c**) and a-axis (**d**) by using a spherical probe exhibiting a radius of 1 Å. The intraframework N-H···O hydrogen bonds are marked by the golden dotted lines. I and II in Figure 2c represent the two types of cavities on the structure.

2.2. Characterizations

The physicochemical behavior of $ZnAtzCO_3$ was measured to investigate its textural characteristics. Fourier transform infrared reflection (FTIR) patterns were performed to further confirm the existence of the carbonate linker. Figure 3a suggests an intense broad band at 1408 cm^{-1} and an additional band at 1310 cm^{-1}, corresponding to the asymmetric stretching modes of carbonate [39]. Besides, the medium band at 850 cm^{-1} was assigned to the bending mode of the carbonate. Figure 3b depicts the powder X-ray diffraction (PXRD) pattern of $ZnAtzCO_3$, which is identical to that derived from SCXRD measurement, indicative of the high purity of the powder sample. In addition, the activation step did not lead to transformation or decomposition of the structure, as suggested by the well-maintained PXRD patterns. Thermogravimetric (TG) analysis in Figure 3c indicates that $ZnAtzCO_3$ is stable up to 500 K, and hence, it holds enough thermal stability for adsorptive separation, which usually requires moderate heating for regeneration. The porosity feature was derived from CO_2 sorption isotherms at 195 K, as shown in Figure 3d. The typical type-I CO_2 isotherms indicated the microporous nature of $ZnAtzCO_3$, giving a Brunauer–Emmett–Teller (BET) surface area of 455.6 m^2/g and a micropore volume of 0.196 cm^3/g.

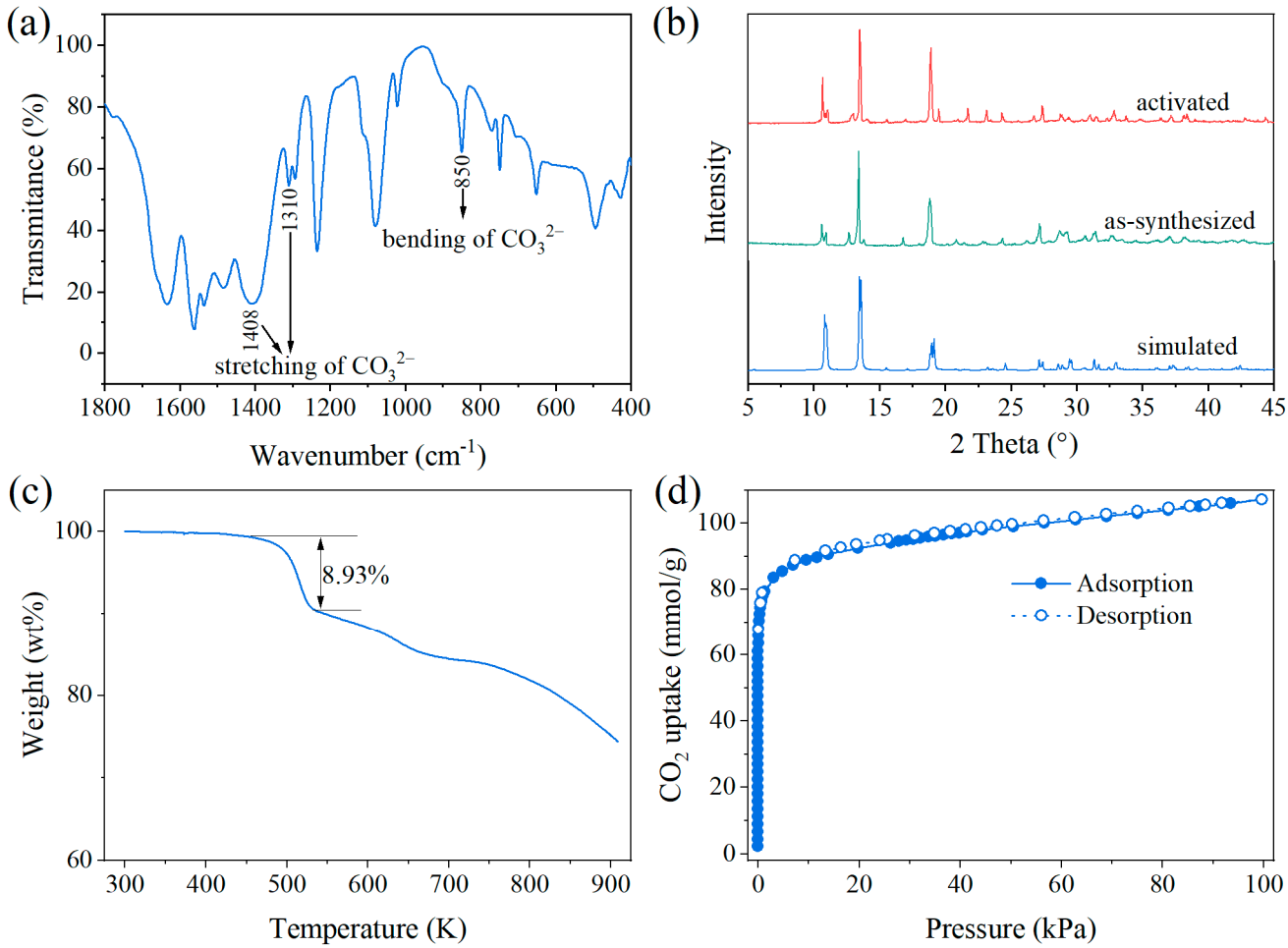

Figure 3. FTIR image (**a**), PXRD patterns (**b**), TG curves (**c**), CO_2 adsorption–desorption isotherms at 195 K (**d**) of $ZnAtzCO_3$.

2.3. Adsorption Equilibrium Behavior of CO_2, N_2, and CH_4

Figure 4a depicts the pure adsorption isotherms of CO_2, N_2, and CH_4 on $ZnAtzCO_3$ at 298 K. It is noticed that CO_2 capacity increased sharply at low pressure, while N_2 and CH_4 uptakes showed a slow increment as the pressure rose. Hence, $ZnAtzCO_3$ showed a significantly higher CO_2 capacity than N_2 and CH_4 between 0–100 kPa. At atmospheric pressure, CO_2 capacity reached as high as 62.8 cm^3/g, while this value for N_2 and CH_4 was 4.3 and 14.7 cm^3/g, respectively. This distinction in adsorption capacity suggests excellent thermodynamic separation for CO_2/N_2 and CO_2/CH_4. Moreover, $ZnAtzCO_3$ demonstrated an exceptional CO_2 adsorption capacity of 44.8 cm^3/g at 15 kPa, highlighting its promising application prospects in low-concentration CO_2 capture, such as CO_2 elimination from the exhaust gas. Moreover, $ZnAtzCO_3$ exhibits a high CO_2 capacity of 56.0 cm^3/g at 50 kPa, indicative of its potential in CO_2 separation with higher CO_2 concentrations, including CO_2 removal from the biogas.

To evaluate the competitive separation of CO_2/CH_4 and CO_2/N_2 on $ZnAtzCO_3$, the IAST selectivities were calculated by means of the IAST model, taking into account the composition of CO_2/N_2 (15:85, *v:v*) and CO_2/CH_4 (50:50,*v:v*) in the exhaust gas and biogas, respectively [40,41]. By incorporating the dual-site Langmuir–Freundlich (DSLF) parameter (Table S1) into the IAST model [42], the IAST selectivities were obtained and shown in Figure 4b. Significantly, CO_2/CH_4 and CO_2/N_2 selectivities are quite high in the whole pressure range of 0–100 kPa. At ambient pressure, the IAST selectivity for CO_2/CH_4 and CO_2/N_2 reached as high as 3538 and 151, respectively, which are comparable to those benchmark MOFs for selective CO_2 capture through thermodynamic separation [12].

Hence, compromised of excellent CO_2 capacity and selectivity, $ZnAtzCO_3$ reveals great potential for selective CO_2 capture.

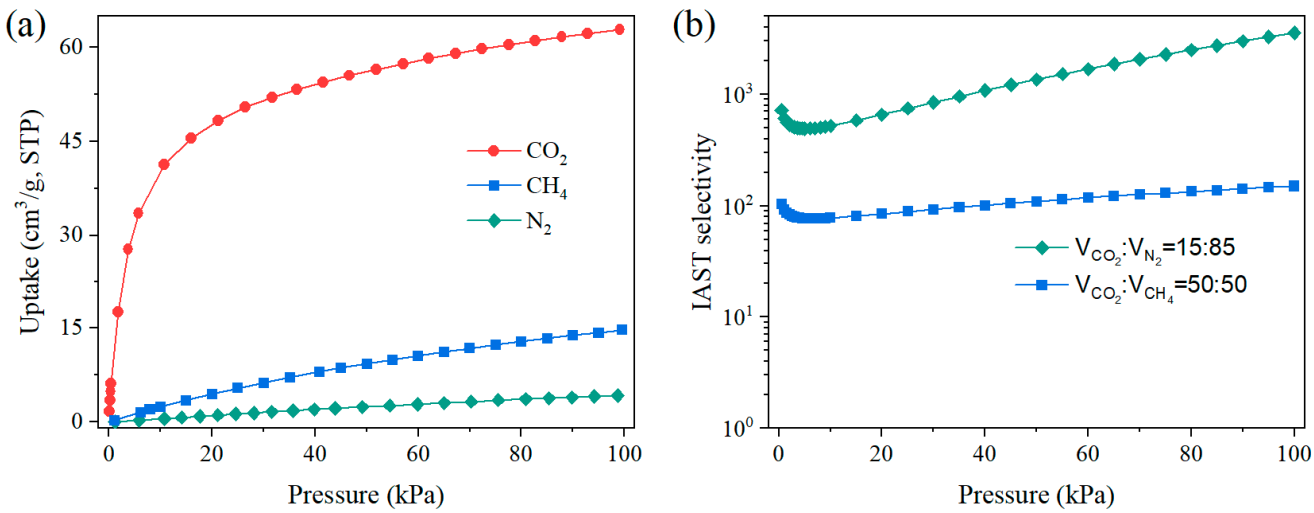

Figure 4. (**a**) Single-component adsorption isotherms of CO_2, N_2 and CH_4 on $ZnAtzCO_3$ at 298 K. (**b**) IAST selectivity of CO_2/N_2 (15:85, *v:v*) and CO_2/CH_4 (15:85, *v:v*) on $ZnAtzCO_3$.

Furthermore, the isosteric heat (Q_{st}) of CO_2, N_2, and CH_4 on $ZnAtzCO_3$, which can be derived from their pure adsorption isotherms at various temperatures (273, 288, and 298 K), is a crucial parameter for determining the adsorption interaction strengths. As shown in Figure 5b, the zero-coverage Q_{st} for the three gases followed an order of CO_2 (32.6 kJ/mol) > CH_4 (22.4 kJ/mol) > N_2 (18.1 kJ/mol), consistent with the dipole moment of the guest molecules (CO_2: 29.1 × 10^{-25} cm^3, CH_4: 25.9 × 10^{-25} cm^3, N_2: 17.4 × 10^{-25} cm^3) [43]. Additionally, it is apparent that the Q_{st} for all gases remained constant between 0–100 kPa, suggesting homogeneity on the pore surface. From the Q_{st} result, we speculate that the remarkable CO_2 selectivity is primarily attributed to its highest adsorption enthalpy.

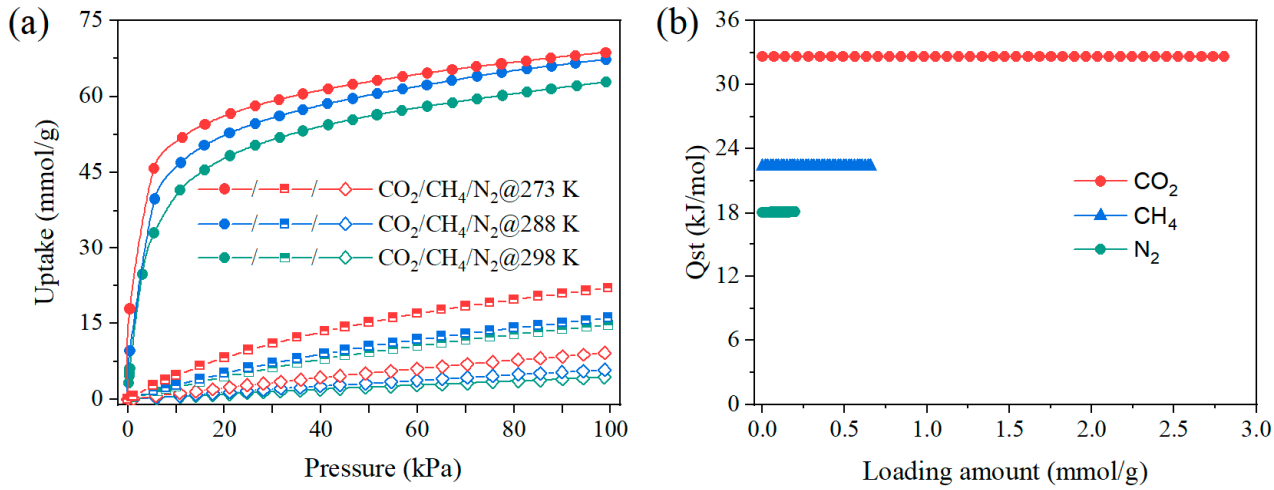

Figure 5. (**a**) Single-component adsorption isotherms of CO_2, N_2, and CH_4 on $ZnAtzCO_3$ at different temperatures (273 K, 288 K, and 298 K). (**b**) Isosteric heat of CO_2, N_2, and CH_4 on $ZnAtzCO_3$.

In addition, $ZnAtzCO_3$ was compared with other MOFs constructed by triazolate linkers on their CO_2 uptake at 15 kPa and 100 kPa, together with the isosteric heat [25,26,29,30,44–47]. As shown in Table 1, the CO_2 uptakes on $ZnAtzCO_3$ exceed those of the ZnF(Tz) series, ZnDatzBdc, $Zn(FA)(datrz)_2$, and $Zn_2(TRZ)_2(BDC)$, and are comparable to that of ZU-301, and slightly lower than those of ZnAtzOx and CALF-20. Hence, $ZnAtzCO_3$ holds comparatively

high CO_2 capacity among these triazolate-based MOFs. Hence, $ZnAtzCO_3$ can be regarded as a promising adsorbent in combination with good capacity and selectivity toward CO_2.

Table 1. Comparisons of CO_2 uptakes at 15 kPa and 50 kPa on typical MOFs constructed by triazolate linkers.

MOFs	Q_{CO2} at 15 kPa (cm^3/g, STP)	Q_{CO2} at 50 kPa (cm^3/g, STP)	Q_{st} (kJ/mol)	T (K)	Ref.
MAF-7	4.5	12.5	25	298	[44]
ZnF(TZ)	6.0	19.1	24	298	[25]
ZnF(daTZ)	21.4	34.1	33	298	[25]
ZnDatzBdc	1.9	5.8	29	298	[30]
CALF-20	53.7	68.3	33.5	303	[26]
ZnAtzOx	60.5	65.0	55	303	[29]
ZU-301	47.7	52.6	39	298	[45]
$Zn(FA)(datrz)_2$	12.3	28.5	24.0	298	[46]
$Zn_2(TRZ)_2(BDC)$	23.5	41.4	-	298	[47]
$Zn_2(TRZ)_2(FA)$	34.7	73.9	-	298	[47]
$ZnAtzCO_3$	44.8	56.0	32.6	298	This work

2.4. Molecular Simulations on the Selective CO_2 Adsorption over N_2 and CH_4

The intrinsic mechanism for the excellent separation performance on $ZnAtzCO_3$ was illustrated by molecular simulations on the preferential adsorption sites, adsorption density distributions, and interaction energy with the aid of Material Studio 7.0 [48]. To visualize the intrinsic host–guest interactions between $ZnAtzCO_3$ and the gas molecules, the preferential interaction site was calculated and depicted in Figure 6. Specifically, for the CO_2 molecule, the carbon atom can form four $C^{\delta+}\cdots^{\delta-}$O-C electrostatic interactions with the oxygen atoms in the carbonate linker, and each oxygen atom can form $O^{\delta-}\cdots^{\delta+}$H-C electrostatic interactions with the hydrogen atoms in the aminotriazolate rings. The multiple host–guest interactions verify that the favorable electrostatic environment of $ZnAtzCO_3$ can form an efficient nanotrap for CO_2. It is noticed that the amine group did not form electrostatic interactions with CO_2, which might originate from insufficient contact with CO_2. For CH_4, CH_4 interacts with three oxygen atoms in the carbonate linker, two nitrogen atoms in the amino groups, and one adjacent triazolate ring through dispersion forces. Considering its significantly smaller polarizability and more inert nature, the preferential site displayed weaker affinity for CH_4 than CO_2. Likewise, being the weakest adsorbate, N_2 forms dispersion interactions with three hydrogen atoms in the aminotriazolate linkers and one oxygen atom in the carbonate linker. From the result above, $ZnAtzCO_3$ shows stronger host–guest interactions with CO_2 compared to N_2 and CH_4.

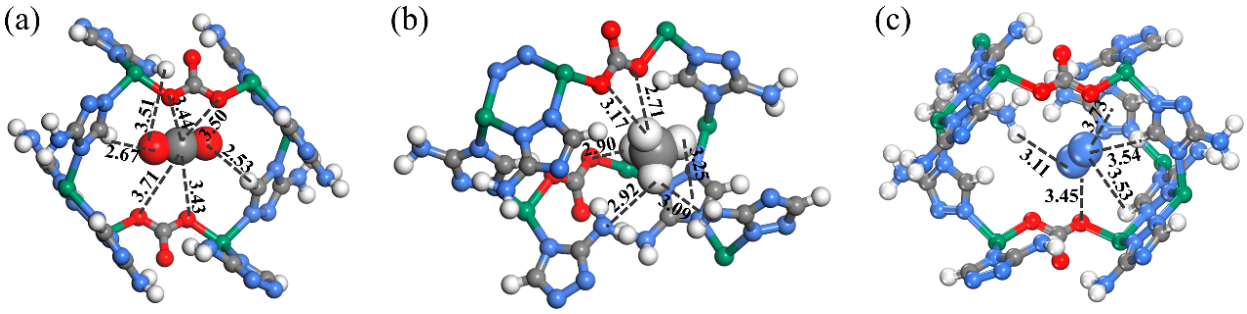

Figure 6. Preferential adsorption sites on the $ZnAtzCO_3$ structure for CO_2 (**a**), CH_4 (**b**), and N_2 (**c**) on $ZnAtzCO_3$. The dashed line represents the host–guest interactions between the $ZnAtzCO_3$ and the gas molecules. The unit of the distance between the gas molecules and the adsorption site is Å.

Figure 7 presents the ambient-temperature adsorption density distributions of the three gases on $ZnAtzCO_3$ at low (15 kPa) and ambient pressure (100 kPa). At both 15 kPa and 100 kPa, the density distribution for CO_2 was the highest, followed by CH_4 and N_2, which is a valid proof of the significantly higher capacity of CO_2 than N_2 and CH_4. As the pressure rose from 15 kPa to 100 kPa, the adsorption density increased for all gases because, generally, the increment in pressure can provide an increasing driving force for gas adsorption.

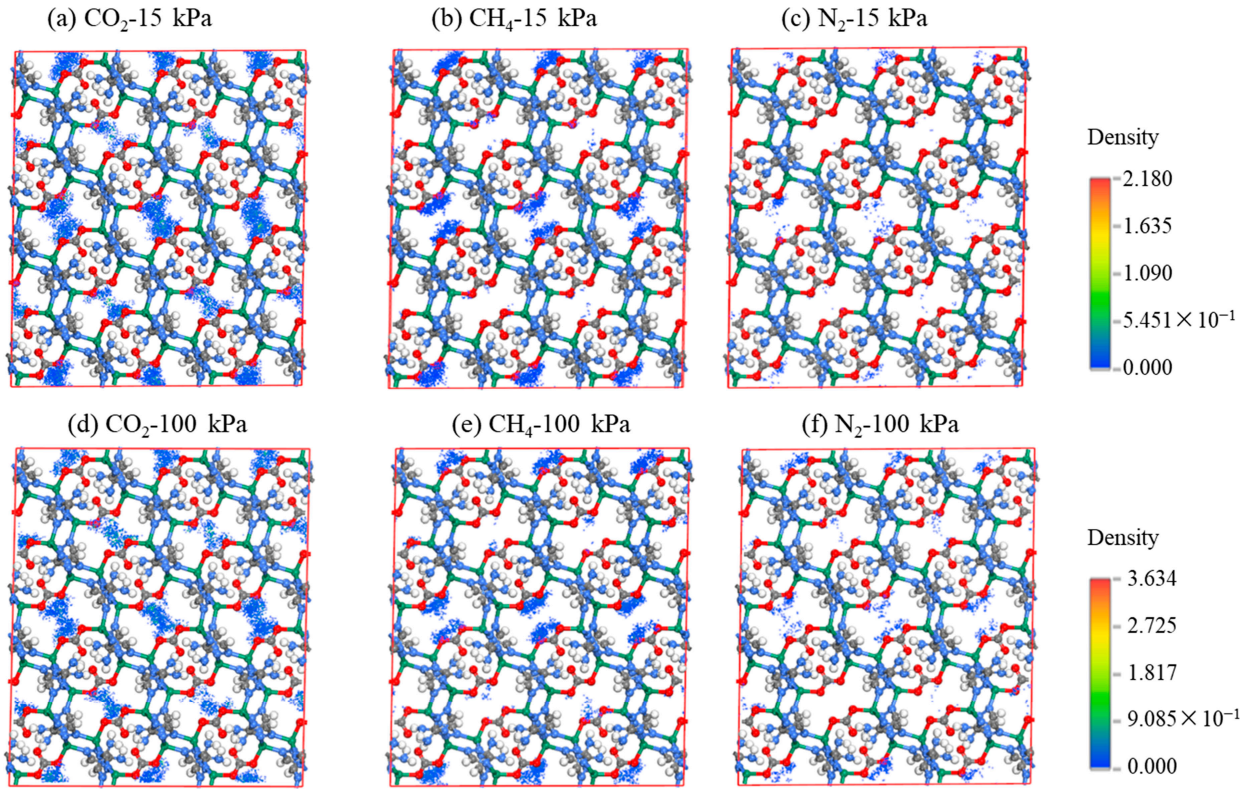

Figure 7. (**a**–**c**) The simulated adsorption density distribution of CO_2, CH_4, and N_2 on $ZnAtzCO_3$ crystal framework at 15 kPa. (**d**–**f**) The simulated adsorption density distribution of CO_2, CH_4 and N_2 on $ZnAtzCO_3$ crystal framework at 100 kPa.

In addition, the distinction of the simulated interaction energy was calculated to further confirm the difference in the adsorption enthalpy. As shown in Figure 8, the average energies between $ZnAtzCO_3$ and the gas molecules were −6.85, −6.06, and −3.50 kcal/mol for CO_2, CH_4, and N_2, respectively, which shows a consistent trend with the Q_{st} result. Hence, the stronger electrostatic host–guest interactions, apparently higher adsorption density distributions, and larger adsorption energy, comprehensively explain the selective CO_2 adsorption over N_2 and CH_4 on $ZnAtzCO_3$.

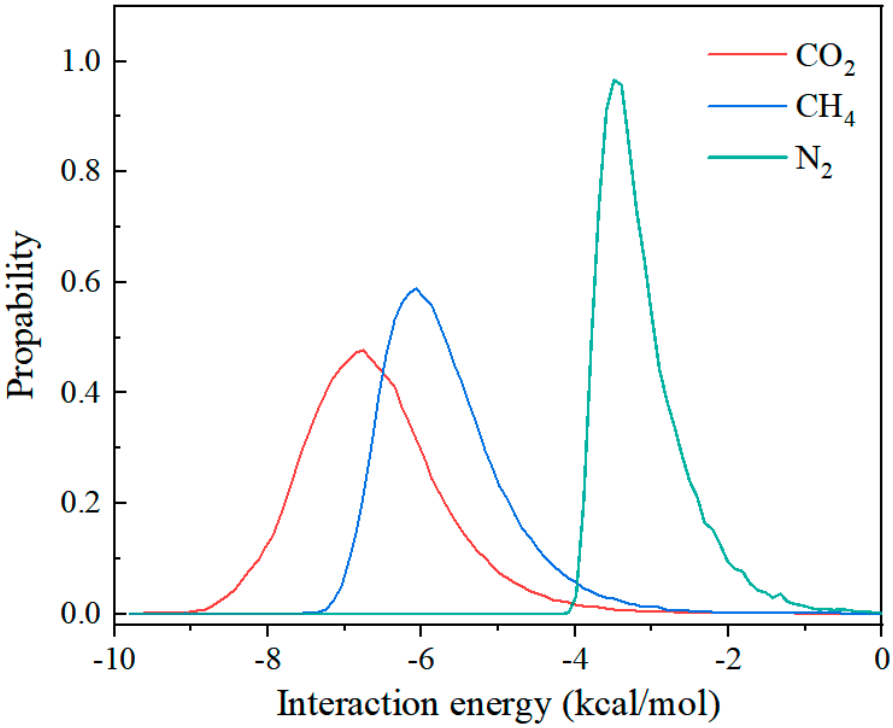

Figure 8. The simulated interaction energy for CO_2, CH_4, and N_2 on $ZnAtzCO_3$.

2.5. Dynamic Breakthrough Experiments

For evaluation of the capability for selective CO_2 capture from the exhaust gas and biogas on $ZnAtzCO_3$, the breakthrough experiments were performed to simulate the dynamic separation performance toward CO_2/N_2 (15:85, *v:v*) and CO_2/CH_4 (50:50, *v:v*) at ambient conditions (Figure 9). It is noticed that CH_4 and N_2 were detected shortly after induction of the gas mixtures and reached equilibrium rapidly, confirming their uptake was inappreciable on $ZnAtzCO_3$. In contrast, CO_2 broke through at 81 min/g and reached equilibrium at 134 min/g for the CO_2/N_2 mixture, and the breakthrough time and equilibrium time for CO_2/CH_4 mixture were 37 and 53 min/g, respectively. In addition, the CO_2 breakthrough time remained constant for five cycles for both mixtures, suggesting their excellent cyclicity in real-world CO_2 capture conditions.

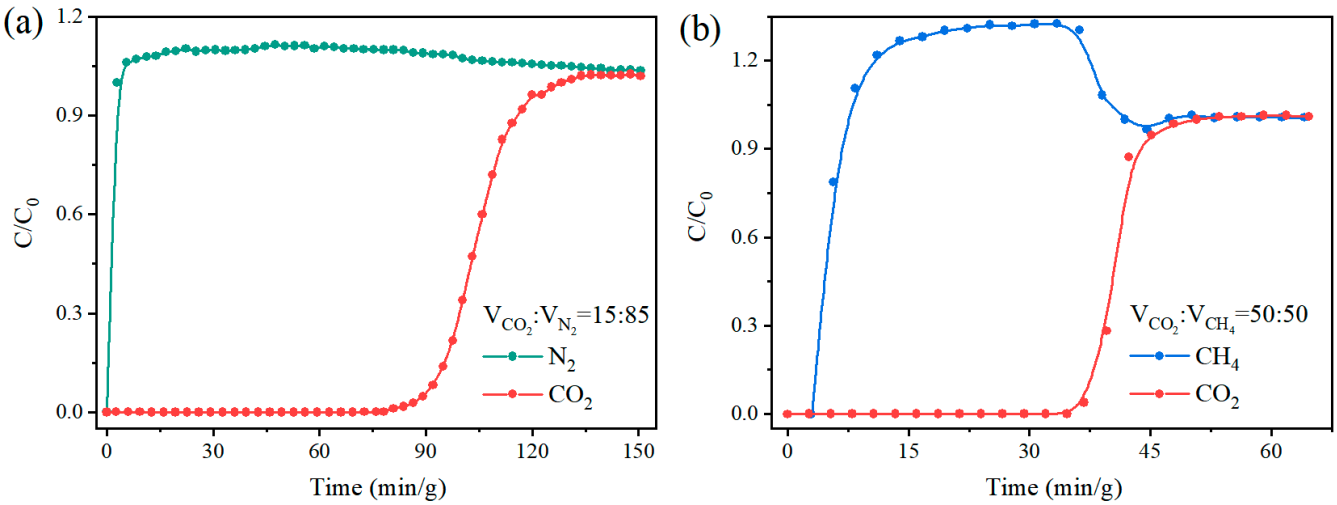

Figure 9. Breakthrough curves for CO_2/N_2 (15:85, *v:v*) (**a**) and CO_2/CH_4 (50:50, *v:v*) (**b**) mixture on $ZnAtzCO_3$ at 298 K and 100 kPa.

3. Materials and Methods

3.1. Material Sources

Zinc sulfate heptahydrate ($ZnSO_4 \cdot 7H_2O$, 99.9%), 3-amino-1*H*-1,2,4-triazole (HAtz, 99.9%), *N*,*N'*-dimethylformamide (DMF, 99.5%), and methanol (MeOH, 99.5%) were supplied by Macklin Biochemical Co., Ltd. (Shanghai, China). The gases employed in this work, including single-component gases (CO_2, CH_4, N_2, and He) of high purity (over 99.9%) and binary gas mixtures of CO_2/N_2 (15:85, *v:v*) and CO_2/CH_4 (50:50, *v:v*), were purchased from Kedi Gas Chemical Industry Co., Ltd. (Foshan, China).

3.2. Synthesis of $ZnAtzCO_3$

HAtz (84.0 mg, 1 mmol) was dispersed in DMF (2 mL) in an autoclave, followed by addition of an aqueous solution (8 mL) of dissolved $ZnSO_4 \cdot 7H_2O$ (287.6 mg, 1 mmol) under stirring. After the suspension was mixed by stirring for 15 min, the autoclave was sealed, kept at 423 K for 60 h, and subsequently slowly cooled to ambient temperature. The resultant colorless crystals were recovered by filtration, washed with deionized H_2O (2 × 20 mL) and MeOH (3 × 20 mL) to remove the unreacted reactants, and then dried in air. The activated $ZnAtzCO_3$ was prepared by heating to remove the contaminants such as DMF, H_2O, and the gases adsorbed from air. CCDC number: 2297804. Crystal Data for $Zn_4C_{10}H_{12}N_{16}O_6$ (M = 713.92 g/mol): triclincic, space group P-1 (no. 2), a = 9.6217(2) Å, b = 9.6316(2) Å, c = 16.3408(4) Å, α = 81.355(2) °, β = 86.938(2)°, γ = 76.093(2)°, V = 1453.01(6) Å^3, Z = 2, T = 150.00(10) K, μ(CuKα) = 0.790 mm^{-1}, D_{calc} = 1.632 g/cm^3, 5103 reflections measured (4.735° $\leq 2\Theta \leq$ 66.988°), 4762 unique (Rint = 0.0381, Rsigma = 0.0300) which were used in all calculations. The final R_1 was 0.0623 (I > 2σ(I)) and wR_2 was 0.1667 (all data). Elemental analysis (wt%) calculated for $Zn_4(Atz)_4(CO_3)_2$ ($Zn_4C_{10}H_{12}N_{16}O_6$): C, 16.83; H, 1.69; N, 31.40; S: 0.00. Found: C, 17.25; H, 2.05; N, 30.5; S, 0.00.

3.3. Characterizations

SCXRD analysis was carried out on a Rigaku Oxford Diffraction (Rigaku, Tokyo, Japan) with a hybrid pixel array detector. Reflections combined with SHELXL corresponding to the crystal class were employed for the calculation of statistics and refinement to solve the non-hydrogen atoms, while the locations and numbers of all hydrogen atoms were calculated theoretically. Elemental analysis was performed on a Vario EL elemental analyzer (Elementar, Langenselbold, Germany) in the CHNS mode. FTIR spectroscopy in the range of 1800–400 cm^{-1} was recorded on a Thermo Scientific iN10 (Thermo Fisher Scientific, Waltham, MA, USA) microscope with potassium bromide as the matrix. PXRD patterns were collected on a Bruker D8 Advance diffractometer (Bruker, Mannheim, Germany). TG measurements of the as-synthesized $ZnAtzCO_3$ were performed on a TGA 550 thermal gravimetric analyzer (Thermo Fisher Scientific, Waltham, MA, USA), and the sample was heated from 303 K to 973 K at a ramping rate of 10 K/min under flowing nitrogen.

3.4. Single-Component Gas Sorption Isotherm Measurements

Single-component sorption isotherm measurements between 0–100 kPa were carried out on 3Flex (Micromeritics, Norcross, GA, USA) at various temperatures. In the preparation process, approximately 100 mg of $ZnAtzCO_3$ was activated under dynamic vacuum for 6 h at 393 K to afford a guest-free sample. During the test, the sample tube was placed in a thermostatic environment by using the ice-acetone bath (195 K) or circulating water bath (288 K, 298 K, and 313 K) to maintain a constant operational temperature.

3.5. Adsorption Selectivity Based on IAST Model

Before the IAST selectivity calculation, the experimental isotherms of CO_2, N_2, and CH_4 require accurate fitting to a mathematical model. In this work, the DSLF equation, based on the assumption that two types of adsorption sites are present in the structure,

was selected and described to describe the adsorption equilibrium of the single-component gases Equation (1) [30,42].

$$q = q_{e1}\frac{k_1 p^{t_1}}{1 + k_1 p^{t_1}} + q_{e2}\frac{k_2 p^{t_2}}{1 + k_2 p^{t_2}} \quad (1)$$

where p is the specific pressure when the gas phase and adsorbed phase reach a steady state; q_{ei} is the saturated uptake of site i; k_i is the affinity coefficients of site i; t_i represents the divergence from an absolute homogeneous surface on site i.

The IAST selectivity for CO_2/N_2 and CO_2/CH_4 on $ZnAtzCO_3$ can be derived according to Equation (2) [40].

$$S_{AB} = \frac{x_A/x_B}{y_A/y_B} \quad (2)$$

where x_i and y_i refer to the volume fractions of component i in the adsorbed phase and the gas phase, separately.

3.6. Isosteric Heat (Qst) Calculation

The experimental adsorption isotherms of CO_2, N_2, and CH_4 on $ZnAtzCO_3$ at various temperatures were fitted to the Virial equation, Equation (3) [49], and the parameters are shown in Table S2.

$$\ln(P) = \ln(\mathrm{N}) + \left(\frac{1}{T}\right)\sum_{i=0}^{m} a_i N^i + \sum_{j=0}^{n} b_j N^j \quad (3)$$

where p is the pressure, N is the gas capacity, T is the absolute temperature, a_i and b_j refer to the corresponding parameter in the Virial equation, while m and n refer to the number required for the accurate fitting of the Virial equation.

Subsequently, the corresponding Q_{st} was figured out by substituting the parameter in the Virial equation into the Clausius–Clapeyron equation, Equation (4) [50].

$$Q_{st} = -R\sum_{i=0}^{m} a_i N^i \quad (4)$$

where R is short for the ideal gas constant, 8.314 J/mol/K.

3.7. Breakthrough Experiments

Dynamic separation experiments of CO_2/N_2 (15:85, *v:v*) and CO_2/CH_4 (50:50, *v:v*) mixtures were performed on self-assembly breakthrough equipment (Figure S3). A small-scale adsorption column was prepared by loading approximately 600 mg of the activated $ZnAtzCO_3$ in a stainless-steel column (Φ 50 × 150 mm). For activation, the column packed with the sample was heated at 393 K for two hours to eliminate the adsorbed contaminants. Subsequently, the column was inserted into the breakthrough equipment and purged by He flow (10 mL/min) at ambient conditions until the baseline was flattened. Finally, the gas was shifted to CO_2/N_2 or CO_2/CH_4 at a flow rate of 3 mL/min. The outlet component was monitored on a thermal conductivity detector (TCD) until the outlet composition reached that of the feed gas, which suggested the breakthrough column reached equilibrium. The adsorption column was recovered by purging He flow at 373 K to liberate the adsorbed gas molecules in the cyclability test.

3.8. Simulation Details

The molecular simulations on the adsorption mechanism were calculated by utilizing the Materials Studio 7.0 software [50]. First, the structures of $ZnAtzCO_3$ and the adsorbates were optimized with the aid of the Forcite and Dmol3 modules. The adsorption characteristics, including the optimal adsorption sites, adsorption density distribution, and stabilized adsorption energy, were simulated in the Sorption module with the Metropolis Monte Carlo method. The adsorption behavior of the guest molecules on $ZnAtzCO_3$ was

described by several motion types, including exchange, conformation, rotation, translation, and regeneration. The Ewald and atom-based methods were employed to depict the electrostatic interaction and Van der Waals interactions between the structure and the guest molecules, respectively. The cutoff for the Metropolis Monte Carlo simulation was set as 12.5 Å. One gas molecule was randomly inserted into the framework in the Location task in the Sorption module, with 1×10^5 steps for equilibrium and production, separately.

4. Conclusions

In conclusion, we propose an interesting type of MOF-based nanotrap, namely $ZnAtzCO_3$, for efficient selective capture of CO_2 from N_2 and CH_4. The favorable electrostatic environment and narrow pore geometry of $ZnAtzCO_3$ show stronger interaction with CO_2 than N_2 and CH_4. Specifically, $ZnAtzCO_3$ accomplished high CO_2 capacities with values of 74.0 cm^3/cm^3 at the fraction of the flue gas (15 kPa) and 91.4 cm^3/cm^3 at the fraction of the biogas (50 kPa), together with ultra-high CO_2/N_2 and CO_2/CH_4 selectivities of 3538 and 151 at ambient conditions, respectively. This excellent separation performance was comprehensively explained by molecular simulations, which suggests that the carbon atom of CO_2 can form strong electrostatic $C^{\delta+}\cdots^{\delta-}O$-C interactions with the oxygen atoms in the carbonate ligand and the oxygen atom of CO_2 can interact with the hydrogen atoms in the triazolate ligand through $O^{\delta-}\cdots^{\delta+}H$-C interactions, enabling $ZnAtzCO_3$ as an optimal nanotrap for CO_2 fixation. Moreover, breakthrough experiments confirm excellent dynamic separation toward CO_2/N_2 and CO_2/CH_4 on $ZnAtzCO_3$, highlighting its potential for selective CO_2 capture. Furthermore, constructing suitable nanotraps with optimal electrostatic environment and pore geometry is worthy of further exploration in other separation circumstances.

Supplementary Materials: The following supporting information can be downloaded at: https://www.mdpi.com/article/10.3390/molecules28237908/s1, Table S1: Fitting parameters of the DSLF model for isotherms of CO_2, N_2, and CH_4 on $ZnAtzCO_3$; Table S2: Fitting parameters and correlation coefficients of the Virial equation for all gases on $ZnAtzCO_3$; Scheme S1: Synthetic pathways for $ZnAtzCO_3$ with starting reactants of $ZnSO_4$/Hatz/DMF/H_2O at 523 K; Figure S1: Asymmetric unit of $ZnAtzCO_3$; Figure S2: Pore size distribution of $ZnAtzCO_3$ based on the HK model using CO_2 as the probe molecule; Figure S3: CO_2 breakthrough times or CO_2/N_2 (*v:v*, 15:85) and CO_2/CH_4 (*v:v*, 15:85) mixtures in five consecutive cycles of breakthrough experiments on $ZnAtzCO_3$.

Author Contributions: Conceptualization, J.P. and D.L.; methodology, J.P. and J.Z.; software, C.D. and J.X.; validation, C.F. and B.Y.; formal analysis, J.P. and J.Z.; investigation, J.P., C.F. and B.Y.; resources, J.X. and C.D.; data curation, J.Z. and C.F.; writing—original draft preparation, J.P.; writing—review and editing, all authors; visualization, J.P., J.Z. and C.D.; supervision, D.L.; project administration, J.P. and D.L.; funding acquisition, J.P., J.X., C.D. and D.L. All authors have read and agreed to the published version of the manuscript.

Funding: This research was funded by National Natural Science Foundation of China (No. 21908069 and 22108034), China Postdoctoral Science Foundation (No. 2020M672636), Guangdong Provincial Natural Science Foundation Project (No. 2023A1515012151), Guangdong Basic and Applied Basic Research Foundation (No. 2023A1515011881), Guangdong-Hong Kong Technology Cooperation Funding Scheme (No. 2023A0505010002), and Scientific Research Project of Guangdong Provincial Department of Education (No. 2022KTSCX122).

Institutional Review Board Statement: Not applicable.

Informed Consent Statement: Not applicable.

Data Availability Statement: Data are contained within the article.

Conflicts of Interest: Author Jiqin Zhong was employed by the company GAC R&D Center, Guangzhou Automobile Group Co., Ltd. The remaining authors declare that the research was conducted in the absence of any commercial or financial relationships that could be construed as a potential conflict of interest.

References

1. Bourzac, K. We have the technology. *Nature* **2017**, *550*, S66–S69. [CrossRef] [PubMed]
2. Schuur, E.A.; McGuire, A.D.; Schädel, C.; Grosse, G.; Harden, J.; Hayes, D.J.; Hugelius, G.; Koven, C.D.; Kuhry, P.; Lawrence, D.M. Climate change and the permafrost carbon feedback. *Nature* **2015**, *520*, 171–179. [CrossRef] [PubMed]
3. Seneviratne, S.I.; Rogelj, J.; Séférian, R.; Wartenburger, R.; Allen, M.R.; Cain, M.; Millar, R.J.; Ebi, K.L.; Ellis, N.; Hoegh-Guldberg, O. The many possible climates from the Paris agreement's aim of 1.5 C warming. *Nature* **2018**, *558*, 41–49. [CrossRef] [PubMed]
4. Majeed, H.; Iftikhar, T.; Ahmad, K.; Qureshi, K.; Tabinda; Altaf, F.; Iqbal, A.; Ahmad, S.; Khalid, A. Bulk industrial production of sustainable cellulosic printing fabric using agricultural waste to reduce the impact of climate change. *Int. J. Biol. Macromol.* **2023**, *253*, 126885. [CrossRef]
5. Trends in Atmospheric Carbon Dioxide. Available online: https://gml.noaa.gov/ccgg/trends/mlo.html (accessed on 10 February 2021).
6. International Energy Agency. *CO2 Emissions in 2022*; International Energy Agency: Paris, France, 2023.
7. Sholl, D.S.; Lively, R.P. Seven chemical separations to change the world. *Nature* **2016**, *532*, 435–437. [CrossRef]
8. Gao, W.; Liang, S.; Wang, R.; Jiang, Q.; Zhang, Y.; Zheng, Q.; Xie, B.; Toe, C.Y.; Zhu, X.; Wang, J. Industrial carbon dioxide capture and utilization: State of the art and future challenges. *Chem. Soc. Rev.* **2020**, *49*, 8584–8686. [CrossRef]
9. Singh, G.; Lee, J.; Karakoti, A.; Bahadur, R.; Yi, J.; Zhao, D.; AlBahily, K.; Vinu, A. Emerging trends in porous materials for CO_2 capture and conversion. *Chem. Soc. Rev.* **2020**, *49*, 4360–4404. [CrossRef]
10. Assunção, L.R.; Mendes, P.A.; Matos, S.; Borschiver, S. Technology roadmap of renewable natural gas: Identifying trends for research and development to improve biogas upgrading technology management. *Appl. Energy* **2021**, *292*, 116849. [CrossRef]
11. Ning, H.; Li, Y.; Zhang, C. Recent progress in the integration of CO_2 capture and utilization. *Molecules* **2023**, *28*, 4500. [CrossRef]
12. Usman, M.; Iqbal, N.; Noor, T.; Zaman, N.; Asghar, A.; Abdelnaby, M.M.; Galadima, A.; Helal, A. Advanced strategies in metal-organic frameworks for CO_2 capture and separation. *Chem. Rec.* **2022**, *22*, e202100230. [CrossRef]
13. Modak, A.; Bhaumik, A. Porous carbon derived via KOH activation of a hypercrosslinked porous organic polymer for efficient CO_2, CH_4, H_2 adsorptions and high CO_2/N_2 selectivity. *J. Solid State Chem.* **2015**, *232*, 157–162. [CrossRef]
14. Kundu, S.K.; Bhaumik, A. Novel nitrogen and sulfur rich hyper-cross-linked microporous poly-triazine-thiophene copolymer for superior CO_2 capture. *ACS Sustain. Chem. Eng.* **2016**, *4*, 3697–3703. [CrossRef]
15. Gao, X.; Yan, W.-H.; Hu, B.-Y.; Huang, Y.-X.; Zheng, S.-M. Porous metal-organic frameworks for light hydrocarbon separation. *Molecules* **2023**, *28*, 6337. [CrossRef] [PubMed]
16. Adil, K.; Belmabkhout, Y.; Pillai, R.S.; Cadiau, A.; Bhatt, P.M.; Assen, A.H.; Maurin, G.; Eddaoudi, M. Gas/vapour separation using ultra-microporous metal-organic frameworks: Insights into the structure/separation relationship. *Chem. Soc. Rev.* **2017**, *46*, 3402–3430. [CrossRef]
17. Yaghi, O.M.; Kalmutzki, M.J.; Diercks, C.S. *Introduction to Reticular Chemistry: Metal-Organic Frameworks and Covalent Organic Frameworks*; John Wiley & Sons: Hoboken, NJ, USA, 2019.
18. Rajendran, A.; Subraveti, S.G.; Pai, K.N.; Prasad, V.; Li, Z. How can (or why should) process engineering aid the screening and discovery of solid sorbents for CO_2 capture? *Acc. Chem. Res.* **2023**, *56*, 2354–2365. [CrossRef]
19. Zhu, M.; Hu, P.; Tong, Z.; Zhao, Z.; Zhao, Z. Enhanced hydrophobic MIL(Cr) metal-organic framework with high capacity and selectivity for benzene VOCs capture from high humid air. *Chem. Eng. J.* **2017**, *313*, 1122–1131. [CrossRef]
20. Ahmad, K.; Nazir, M.A.; Qureshi, A.K.; Hussain, E.; Najam, T.; Javed, M.S.; Shah, S.S.A.; Tufail, M.K.; Hussain, S.; Khan, N.A.; et al. Engineering of zirconium based metal-organic frameworks (Zr-MOFs) as efficient adsorbents. *Mater. Sci. Eng. B* **2020**, *262*, 114766. [CrossRef]
21. Zhang, Z.; Yao, Z.-Z.; Xiang, S.; Chen, B. Perspective of microporous metal-organic frameworks for CO_2 capture and separation. *Energy Environ. Sci.* **2014**, *7*, 2868–2899. [CrossRef]
22. Kim, Y.; Huh, S. Pore engineering of metal-organic frameworks: Introduction of chemically accessible lewis basic sites inside mof channels. *Cryst. Eng. Comm.* **2016**, *18*, 3524–3550. [CrossRef]
23. He, T.; Kong, X.-J.; Li, J.-R. Chemically stable metal-organic frameworks: Rational construction and application expansion. *Acc. Chem. Res.* **2021**, *54*, 3083–3094. [CrossRef]
24. Chen, Z.; Kirlikovali, K.O.; Shi, L.; Farha, O.K. Rational design of stable functional metal-organic frameworks. *Mater. Horiz.* **2023**, *10*, 3257–3268. [CrossRef] [PubMed]
25. Shi, Z.; Tao, Y.; Wu, J.; Zhang, C.; He, H.; Long, L.; Lee, Y.; Li, T.; Zhang, Y.-B. Robust metal–triazolate frameworks for CO_2 capture from flue gas. *J. Am. Chem. Soc.* **2020**, *142*, 2750–2754. [CrossRef] [PubMed]
26. Lin, J.-B.; Nguyen, T.T.T.; Vaidhyanathan, R.; Burner, J.; Taylor, J.M.; Durekova, H.; Akhtar, F.; Mah, R.K.; Ghaffari-Nik, O.; Marx, S.; et al. A scalable metal-organic framework as a durable physisorbent for carbon dioxide capture. *Science* **2021**, *374*, 1464–1469. [CrossRef] [PubMed]
27. Nguyen, T.T.T.; Lin, J.-B.; Shimizu, G.K.H.; Rajendran, A. Separation of CO_2 and N_2 on a hydrophobic metal organic framework CALF-20. *Chem. Eng. J.* **2022**, *442*, 136263. [CrossRef]
28. Vaidhyanathan, R.; Iremonger, S.S.; Dawson, K.W.; Shimizu, G.K. An amine-functionalized metal organic framework for preferential CO_2 adsorption at low pressures. *Chem. Commun.* **2009**, *35*, 5230–5232. [CrossRef] [PubMed]
29. Banerjee, A.; Nandi, S.; Nasa, P.; Vaidhyanathan, R. Enhancing the carbon capture capacities of a rigid ultra-microporous mof through gate-opening at low CO_2 pressures assisted by swiveling oxalate pillars. *Chem. Commun.* **2016**, *52*, 1851–1854. [CrossRef]

30. Peng, J.; Liu, Z.; Wu, Y.; Xian, S.; Li, Z. High-performance selective CO_2 capture on a stable and flexible metal-organic framework via discriminatory gate-opening effect. *ACS Appl. Mater. Interfaces* **2022**, *14*, 21089–21097. [CrossRef]
31. Ye, Y.; Xian, S.; Cui, H.; Tan, K.; Gong, L.; Liang, B.; Pham, T.; Pandey, H.; Krishna, R.; Lan, P.C.; et al. Metal-organic framework based hydrogen-bonding nanotrap for efficient acetylene storage and separation. *J. Am. Chem. Soc.* **2022**, *144*, 1681–1689. [CrossRef]
32. Niu, Z.; Cui, X.; Pham, T.; Verma, G.; Lan, P.C.; Shan, C.; Xing, H.; Forrest, K.A.; Suepaul, S.; Space, B.; et al. A MOF-based ultra-strong acetylene nano-trap for highly efficient C_2H_2/CO_2 separation. *Angew. Chem. Inter. Ed.* **2021**, *60*, 5283–5288. [CrossRef]
33. Wen, H.-M.; Liu, M.; Ling, Y.; Gu, X.-W.; Liu, D.; Yu, C.; Liang, Y.; Xie, B.; Li, B.; Hu, J. A metal-organic framework based propylene nano-trap with dual functionalities for highly efficient propylene/propane separation. *J. Mater. Chem. A* **2023**, *11*, 17821–17827. [CrossRef]
34. Zhu, H.; Wang, Y.; Wang, X.; Fan, Z.-W.; Wang, H.-F.; Niu, Z.; Lang, J.-P. Design of a MOF-based nano-trap for the efficient separation of propane from propylene. *Chem. Commum.* **2023**, *59*, 5757–5760. [CrossRef]
35. Chen, Y.; Qiao, Z.; Lv, D.; Duan, C.; Sun, X.; Wu, H.; Shi, R.; Xia, Q.; Li, Z. Efficient adsorptive separation of C_3H_6 over C_3H_8 on flexible and thermoresponsive CPL-1. *Chem. Eng. J.* **2017**, *328*, 360–367. [CrossRef]
36. Zhang, P.; Yang, L.; Liu, X.; Wang, J.; Suo, X.; Chen, L.; Cui, X.; Xing, H. Ultramicroporous material based parallel and extended paraffin nano-trap for benchmark olefin purification. *Nat. Commun.* **2022**, *13*, 4928. [CrossRef] [PubMed]
37. Basnayake, S.A.; Su, J.; Zou, X.; Balkus, K.J., Jr. Carbonate-based zeolitic imidazolate framework for highly selective CO_2 capture. *Inorg. Chem.* **2015**, *54*, 1816–1821. [CrossRef]
38. Lin, Y.-Y.; Zhang, Y.-B.; Zhang, J.-P.; Chen, X.-M. Pillaring Zn-triazolate layers with flexible aliphatic dicarboxylates into three-dimensional metal-organic frameworks. *Cryst. Growth Des.* **2008**, *8*, 3673–3679. [CrossRef]
39. Frost, R.L.; Martens, W.N.; Wain, D.L.; Hales, M.C. Infrared and infrared emission spectroscopy of the zinc carbonate mineral smithsonite. *Spectrochim. Acta Part A* **2008**, *70*, 1120–1126. [CrossRef] [PubMed]
40. Myers, A.L.; Prausnitz, J.M. Thermodynamics of mixed-gas adsorption. *AIChE J.* **1965**, *11*, 121–127. [CrossRef]
41. Walton, K.S.; Sholl, D.S. Predicting multicomponent adsorption: 50 years of the ideal adsorbed solution theory. *AIChE J.* **2015**, *61*, 2757–2762. [CrossRef]
42. Peng, J.; Zhong, J.; Liu, Z.; Xi, H.; Yan, J.; Xu, F.; Chen, X.; Wang, X.; Lv, D.; Li, Z. Multivariate metal-organic frameworks prepared by simultaneous metal/ligand exchange for enhanced c2–c3 selective recovery from natural gas. *ACS Appl. Mater. Interfaces* **2023**, *15*, 41466–41475. [CrossRef]
43. Li, J.-R.; Kuppler, R.J.; Zhou, H.-C. Selective gas adsorption and separation in metal-organic frameworks. *Chem. Soc. Rev.* **2009**, *38*, 1477–1504. [CrossRef]
44. Zhang, J.-P.; Zhu, A.-X.; Lin, R.-B.; Qi, X.-L.; Chen, X.-M. Pore surface tailored sod-type metal-organic zeolites. *Adv. Mater.* **2011**, *23*, 1268–1271. [CrossRef] [PubMed]
45. Yu, C.; Ding, Q.; Hu, J.; Wang, Q.; Cui, X.; Xing, H. Selective capture of carbon dioxide from humid gases over a wide temperature range using a robust metal-organic framework. *Chem. Eng. J.* **2021**, *405*, 126937. [CrossRef]
46. Xing, G.E.; Liu, Q.; Zhang, Y.; Zhang, S.; Dong, Y. Microporous zinc(ii) metal-organic framework with 6-connected pcu topology: Synthesis, structure, and gas adsorption properties. *Z. Anorg. Allg. Chem.* **2015**, *641*, 1556–1559. [CrossRef]
47. Zhai, Q.-G.; Bai, N.; Li, S.N.; Bu, X.; Feng, P. Design of pore size and functionality in pillar-layered zn-triazolate-dicarboxylate frameworks and their high CO_2/CH_4 and C_2 hydrocarbons/CH_4 selectivity. *Inorg. Chem.* **2015**, *54*, 9862–9868. [CrossRef]
48. *Materials Studio, v7.0*, Biovia Software Inc.: San Diego, CA, USA, 2013.
49. Czepirski, L.; JagieŁŁo, J. Virial-type thermal equation of gas-solid adsorption. *Chem. Eng. Sci.* **1989**, *44*, 797–801. [CrossRef]
50. Nuhnen, A.; Janiak, C. A practical guide to calculate the isosteric heat/enthalpy of adsorption via adsorption isotherms in metal-organic frameworks, mofs. *Dalt. Trans.* **2020**, *49*, 10295–10307. [CrossRef]